Dimensions, texture-distribution and geochemical heterogeneities of fracture-related dolomite geobodies hosted in Ediacaran limestones, northern Oman

Veerle Vandeginste[1*], Cédric M. John[1], John W. Cosgrove[1], Christina Manning[2]

[1]Department of Earth Science and Engineering and Qatar Carbonate and Carbon Storage Research Centre, Imperial College London, London SW7 2BP, UK

[2]Department of Earth Sciences, Royal Holloway University of London, Egham Hill, Egham, Surrey TW20 0EX, UK

[*]Corresponding author: v.vandeginste@imperial.ac.uk

Keywords:

Clumped isotopes, dolomitization, geobody, heterogeneity, stable carbon and oxygen isotopes

ABSTRACT

Predicting spatial distribution, dimension, and geometry of diagenetic geobodies as well as heterogeneities within these bodies is challenging in subsurface applications, and it can impact the results of reservoir modelling. In this outcrop-based study we generated a data set of dimensions of fracture-related dolomite geobodies hosted in Ediacaran (Khufai Formation) limestones of the Oman Mountains that are up to several hundreds of meters long and up to a few tens of meters wide. The dolomite formed under burial conditions by fluids that interacted with siliciclastic layers as demonstrated by the enriched Fe (up to 4.4%) and Mn (up to 0.8%) contents and $^{87}Sr/^{86}Sr$ (~0.710) signatures. Dolomitization probably occurred during the Hercynian Orogeny (or pre-Permian time) based on the fact that dolomitization predates some folding and occurred in between the onset and termination of bedding-parallel stylolitization, and hence, most likely before the deep burial related to the Alpine Orogeny and the fact that pre-Permian rocks have been affected by intense deformation related to the Hercynian Orogeny during Carboniferous time. The clumped isotope signature yields a temperature of about 260ºC, interpreted as the apparent equilibrium temperature obtained during uplift after deepest burial during the Late Cretaceous. Lateral transects across the dolomite bodies show that zebra dolomite textures are common throughout the body and that vugs are more common at the rim than the center of the bodies. Moreover, there is a weak geochemical trend with more depleted ^{18}O, Fe and Mn concentrations in the core than at the rim of the dolomite bodies. These results show that there are minor heterogeneities within the dolomite bodies investigated. These data contrast with previous studies, where more significant variation in width of the dolomitization halo and texture is reported for larger dolomite bodies which formed in more permeable host rocks than the examples from the Oman Mountains.

INTRODUCTION

Estimating the dimension of diagenetic geobodies from core data is a difficult task in the subsurface and has important impacts on the accuracy of reservoir models. Some predictive rules have been suggested for the dimension of depositional geobodies, such as fluvial geobodies (Lunt et al., 2013; Pranter et al., 2009), and grainstone bodies (Harris et al., 2011). However, data on dimensions and geometries of diagenetic geobodies is scarce. Diagenetic geobodies are generally templated by the depositional facies, as well as the earlier diagenetic phases, and the distribution of fractures (Vandeginste et al., 2013b). As such, predicting the spatial distribution, dimension, and geometry of diagenetic geobodies is even more challenging than for sedimentary geobodies. A larger outcrop data set on dimensions and textural variability of fracture-related dolomite geobodies, resulting from a common diagenetic process in carbonates, may help constrain the relative importance and interaction of the different controlling factors on the geobody distribution and dimension.

Correctly estimating the size, distribution, and permeability of geobodies in reservoir models is essential to constrain flow behaviors. At the reservoir scale, heterogeneity is influenced by the variability in geobodies and their respective petrophysical properties, but the geobodies themselves can be heterogeneous on a smaller scale. Several studies document heterogeneity within fracture-related geobodies with respect to porosity, permeability, and textures (Dewit et al., 2012; Lapponi et al., 2011; Shah et al., 2010; Sharp et al., 2010; Wilson et al., 2007). However, the results of previous studies may not be applicable for fracture-related dolomite bodies of other dimensions (such as smaller geobodies).

This study investigates the dimension of fracture-related dolomite bodies hosted in Ediacaran limestone of the Khufai Formation in Wadi Bani Awf (central Oman Mountains). In addition to constraining dimensions, the textural and geochemical heterogeneities are assessed by evaluating data along transects across the dolomite geobodies. The goals of this paper are to: (a) construct a data set of dimensions of fracture-related dolomite bodies in Wadi Bani Awf; (b) gain insight in the dolomitization process, including structural framework, origin of dolomitizing fluids, as well as, the timing of dolomitization; and, (c) investigate spatial and temporal changes in diagenetic patterns.

GEOLOGICAL SETTING

Oman is situated at the eastern edge of the Arabian Plate. Samples for this study were collected at Wadi Bani Awf in the center of the Jebel Akhdar dome, a tectonic window in north Oman (Fig. 1A,B). Here, Precambrian to Cretaceous autochthonous rocks crop out between the oceanic allochthon, i.e. the Hawasina volcano-sedimentary nappe complex, and the overlying Semail ophiolite exposed in the Oman Mountains (Poupeau et al., 1998). The emplacement of nappes and NE-directed subduction of the Arabian plate are the result of the Alpine Orogeny (Boudier et al., 1985; Breton et al., 2004; Hacker, 1994).

The sediments immediately overlying crystalline basement consist of the Precambrian Abu Mahara Group, followed by the Nafun Group I containing the Hadash and Masirah Bay Formations (Fig. 1C) comprised of diamictite, greywacke and feldspathic sandstone, and the Khufai Formation comprised of black fetid limestone and dolomite with stromatolitic laminations (Béchennec et al., 1993). The Khufai Formation (or Hajir Formation) forms the focus of this study and was deposited in a proximal progradational ramp system in the Huqf area and a more distal system in Jebel Akhdar (Allen, 2007; Le Guerroue et al., 2006a; Wright et al., 1990). The Abu Mahara Group and Nafun Group I developed during intra-continental extension, probably associated with crustal thinning subsequent to the early Panafrican Orogeny (Genna et al., 2002). The Khufai Formation is capped by a disconformity surface, and overlain by the Nafun Group II with the Shuram Formation (or Mu'aydin Formation; finely laminated siltstone) and the Buah Formation (or the Kharus Formation; black limestone, red siltstone and some dolomite; Fig. 1C). This is followed by the Ara Group with the Fara Formation (ignimbrite and tuffite, sandstone and siltstone and some limestone and dolomite; Fig. 1C). The Fara Formation is truncated at the top by a regional unconformity that marks the base of the Upper Permian succession, and reflects intense erosion that may be associated with moderate compression during late Panafrican tectonism (Béchennec et al., 1993) or the Hercynian Orogeny (Faqira et al., 2009).

METHODOLOGY

Seven transects were sampled (by drilling 2 inch diameter cores) across the fracture-related dolomite bodies, easily recognized in the field by their red weathering color contrasting with the black limestone of the Khufai Formation host rock in Wadi Bani Awf (Fig. 1D). The main sampling sites are the outcrops in the center of Wadi Bani Awf (around N23º12.63' E57º23.43'), but also some samples were collected and observations made in the more northern side of Wadi Bani Awf (N23º15.25' E57º23.82'). By analyzing transects across dolomite bodies, one can evaluate not only the difference between limestone and dolomite, but also the lateral and textural variation within the dolomite bodies. The dimensions of the dolomite bodies were measured on Google Earth satellite images and, also, selectively in the field. A fracture analysis was carried out on two representative beds by recording the strike, dip, aperture, filling, distance, and geometry of the fractures and veins. The structural data were plotted onto stereographic projections using Orient version 2.1.2 (2012), a freeware by F.W. Vollmer.

We collected and investigated 80 hand specimens. Rock slabs were cut and finely polished using silicon carbide grit 220 and subsequently grit 600. The polished surfaces of the slabs and thin sections halves were etched with 1M HCl and stained with Alizarin Red S and potassium ferricyanide to distinguish calcite and dolomite, and their ferroan equivalents following a procedure modified from Dickson (1966).

A total of 79 thin sections were examined using a Zeiss Axioskop 40 polarization microscope (with a connected Zeiss Axiocam ICc1 digital camera for photomicrographs) and a CITL Cathodoluminescence Mk5-2 stage mounted on a Nikon Eclipse 50i microscope (with an attached Nikon DS-Fi1c digital camera) for cathodoluminescence (CL) microscopy. Operating conditions for the CL stage were about 200 µA and 13 kV. The CL color descriptions reported in the results are based on unstained thin sections halves.

Small rock pieces of all 80 samples were cut, cleaned with distilled water, dried overnight and then crushed to a fine powder using an agate mortar and pestle. One to two grams of these powders were used for X-ray diffraction analyses, following the procedure described in Vandeginste et al. (2013b), to determine the mineralogy and to derive semi-quantitative information on calcite and dolomite contents. Subsequently, 250 mg of each carbonate sample powder of either dolomite or calcite (>95% pure based on XRD) was dissolved in 5% HNO_3 in preparation of ICP-AES analysis to determine elemental composition following a procedure described in Vandeginste et al. (2013b). As an additional test, the ICP-AES results were compared with geochemical data obtained by microprobe analyses on a few thin sections (CAMECA SX-100 electron microprobe at the University of Montpellier II, France) following analysis correction based on Merlet (1994). The microprobe results were consistent with the ICP-AES data.

Carbonate samples (100 to 150 µg) for stable carbon and oxygen isotope analyses were taken with a dental drill, which enabled sampling of specific diagenetic phases.

In addition, nine representative samples of both limestone and dolomite were treated with a Calgon-H_2O_2 solution with the aim of assessing and subsequently ruling out any effect of organic matter or clays on the stable carbon and oxygen isotopic composition of the carbonates. The carbonate powders were reacted with phosphoric acid in a Thermo Scientific automated Kiel IV carbonate device at 70ºC, and the resulting CO_2 gas was analyzed in a MAT253 mass spectrometer in the Qatar Stable Isotope lab at Imperial College London. The carbon and oxygen isotopic values for carbonate samples are reported in per mil notation relative to Vienna Pee Dee Belemnite (VPDB). Measurements of NBS19 and internal lab (Carrara Marble) standards allowed for the correction of instrumental drift. Replicate analysis of these standards showed a reproducibility of 0.06‰ for $\delta^{13}C$ and 0.12‰ for $\delta^{18}O$ (2σ standard deviation). Dolomite $\delta^{18}O$ was corrected using the acid fractionation factors given by Rosenbaum and Sheppard (1986) and Kim et al. (2007).

Aliquots of 5 to 8 mg of dolomite per replicate were used for clumped isotope analysis. Three to five replicates per sample were measured on a total of 4 dolomite samples. For each replicate, the dolomite powders were reacted for 20 minutes with phosphoric acid in a reaction vessel that was kept at a temperature of 90ºC by a heated water bath on a hot plate. The resulting CO_2 was trapped in a liquid nitrogen trap during the time of reaction. The liquid nitrogen trap was subsequently replaced by a slush trap (containing ethanol and liquid nitrogen) which was kept at a temperature of about -80ºC to release the CO_2, but not water. The CO_2 gas went through Poropak trap maintained at -35˚C for about 40 to 60 minutes till the pressure in the slush trap was down to baseline pressure. During this Poropak transfer, CO_2 was collected by a liquid nitrogen trap after the Poropak trap. Finally, CO_2 was trapped in a cold finger, and if results on mass 48 offset (Huntington et al., 2009) indicated contamination the entire aliquot of gas was used for a second identical cleaning process.

Two mass spectrometers (Pinta and Niña) were used during the course of these measurements. The gas from the cold finger was introduced into the instrument and measured by 8 acquisitions of 7 cycles. The quality of the data was checked for outliers, and the reliability of the measurements (and 47 mass data) was evaluated using the mass 49 index and the mass 48 offset (Huntington et al., 2009): samples with a mass 49 index above 0.3 and/or which fall outside of 2 standard deviation in mass 48 from the heated gas line were rejected. Standards, Carrara Marble and ETH3, and heated gas were measured each generally twice a week and were used to correct for non-linearity of the mass spectrometer, and the data presented here is in the Carbon Dioxide Equilibrated Scale (CDES) of Dennis et al. (2011).

The strontium isotopic composition was also determined from a selection of samples that were used for stable carbon and oxygen analyses. The method of chemical preparation to separate Sr and the measurements on the mass spectrometer at Royal Holloway University London (UK) follow that described in Vandeginste et al. (2013a).

Fluid inclusions were studied in six doubly polished wafers (prepared without using a hot plate and collected from 10-15 cm long drilled cores) on a Linkam THMSG600 heating-cooling stage. Calibration of the stage was performed by measuring phase changes in synthetic fluid inclusions of known composition. Repeatability of the final melting temperature of ice (Tm) is within 0.2ºC and of the homogenization temperature (Th) within 2ºC for measurements in the studied carbonate wafers.

RESULTS

Dimension and structural characterization of fracture-related dolomite geobodies

The dolomite geobodies have reddish weathering colors (Fig. 2A-D). The geobodies crosscut limestone beds generally at a steep angle (Fig. 2A, B). However, some parts of small dolomite bodies can also occur parallel to bedding (Fig. 2C). Most dolomite bodies are slightly curved (Fig. 2D). The Khufai Formation beds are folded (mainly at larger scale) with the beds dipping vertically at some sites. Some N-S and E-W faults occur at the main sampling site and place the overlying Shuram Formation siliciclastics adjacent to the Khufai Formation limestone. There is no dolomite present along those faults. A total of 222 discontinuous (as seen at the surface) dolomite geobodies were mapped in an area of about 10 square kilometers (3.9 square miles) on Google Earth satellite images (Fig. 1D). Image analysis reveals that the strike of these bodies is predominantly NNE-SSW to NE-SW (Fig. 3A). Detailed structural analyses on the outcrop (sections BAC and BAG) show that red dolomite veins are subvertical west-dipping with NNE-SSW strike, whereas white calcite veins (crosscutting the other vein set) have a NE-SW or ENE-WSW strike (Fig. 3B, C). Rare NW-trending veins consist of dolomite, calcite, or both. The strike of the bedding at the sampling sites is N-S and the dip is not more than 16º to 30º to the east. The dolomite geobodies vary widely in length between 3 to 636 m (10 to 2087 ft) but less in width, i.e. between 1 to 60 m (3 to 197 ft), based on measurements on Google Earth satellite images and confirmed with select field measurements. The length/width aspect ratio of the dolomite bodies varies from 0.4 to 112. There is thus no clear correlation between length and width of the bodies, as indicated by a correlation coefficient of 0.1 (Fig. 4A). The histogram of length of the geobodies shows a higher occurrence of shorter geobodies (three bins for length up to 75 m [246 ft]), although the average geobody length is 97 m (318 ft; Fig. 4B). Also, the histogram of width shows the highest distribution for the three bins of smallest width, i.e. up to 7.5 m (25 ft) wide, whereas the average width of the bodies is 7 m (23 ft; Fig. 4C).

Macroscopic and petrographic characteristics of host rock and fracture-related dolomite

The limestone host rock consists of medium sized calcite crystals that have wide (up to 25 µm) cleavage twin planes. Only a faint relict of the original texture is visible (Fig. 5A). This limestone texture (a recrystallized peloidal grainstone) is the same in all seven transects. Rare, small authigenic albite crystals are present within the limestone (but not in the dolomite). The fracture-related dolomite is mainly composed of zebra dolomite in which grey fine-crystalline and white coarse-crystalline dolomite bands alternate (Fig. 2E, F). Some dolomite samples also have a brownish fine-crystalline zone. The zebra bands are generally parallel to bedding, but some bands are oblique, and some white dolomite zones are perpendicular to bedding (Fig. 2F). The dolomite crystals display wide cleavage twin planes that are straight or bent, and crosscutting each other. The center of the white dolomite bands contain saddle dolomite crystals with curved outline and sweeping extinction under crossed polarized light. On top of these saddle dolomites, former pore space is filled with calcite cement. In general, calcite cements in pore spaces in the center of white dolomite zones or in vugs (Fig. 2G) are more abundant at the rim (close to contact with limestone) than in the center of fracture-related dolomite bodies. At the intersection of two fracture-related dolomite bodies, white dolomite bands tend to be thicker and have a more heterogeneous orientation. Although thin red dolomite is present along bedding parallel stylolites in the limestone (Fig. 2H), bedding parallel stylolites also crosscut dolomite (Fig. 5B). A few samples show some brown iron oxidation stains (Fig. 5C). The white dolomite underlying this altered band is homogeneous and displays dark red luminescence under CL, whereas the dolomite overlying this band has alternating inclusion-rich and inclusion-poor zones. The latter zones also exhibit a zoned CL pattern (Fig. 5D).

Geochemistry of host rock and fracture-related dolomite

Major and minor element geochemistry

The dolomite is nearly stoichiometric (50 to 52 mole% $CaCO_3$), based on XRD measurements. Limestone and dolomite differ in Mg content (10.2 to 12.6 wt% for dolomite, 0.1 to 0.6 wt% for limestone). Also the Fe and Mn content is different, i.e. enriched in dolomite (Fe: 10834 to 44329 ppm, Mn: 2354 to 7888 ppm) and depleted in limestone (Fe: 23 to 1027 ppm; Mn: 44 to 720 ppm; Fig. 6). In contrast, the Al and K, and acid insoluble residue (IR) are similar in both the limestone (Al: 21 to 119 ppm, K: 51 to 158 ppm, IR: 1.8 to 6.5 wt%) and dolomite (Al: 35 to 160 ppm, K: 51 to 154 ppm, IR: 1.0 to 10.7 wt%). The Fe content in the fracture-related dolomite is generally higher near the rims of the dolomite body than in the center (Fig. 7).

Stable isotopes of carbon and oxygen

The Precambrian limestone samples collected from the Khufai Formation have $\delta^{18}O$ values ranging from -11.9 to -9.4‰ VPDB and $\delta^{13}C$ values ranging between +6.3 and +7.6‰ VPDB. The fracture-related dolomite samples in our study have a more negative $\delta^{18}O$ than that of the limestone, and the $\delta^{13}C$ signature in dolomite varies from +3.7 to +7.4‰ VPDB compared to +6.3 to +7.6‰ VPDB in limestone (Fig. 8).

The fine-crystalline dolomite ($\delta^{18}O$: -14.7 to -11.9‰ VPDB and $\delta^{13}C$: +4.0 to +7.4‰ VPDB) has a similar stable isotopic signature as the coarse-crystalline dolomite ($\delta^{18}O$: -15.2 to -12.2‰ and $\delta^{13}C$: +3.7 to +7.0‰). The highest $\delta^{18}O$ and $\delta^{13}C$ values measured in the dolomite are similar to those of calcite cement ($\delta^{18}O$ values from -14.6 to -12.3‰ and $\delta^{13}C$ value between +2.9 to +4.5‰) filling vugs and pore space in the center of coarse dolomite bands. The $\delta^{18}O$ and $\delta^{13}C$ values along cross-dolomite transects show no correlation between the $\delta^{13}C$ signature and distance from the core of the fracture-related dolomite body, whereas $\delta^{18}O$ values show a weak trend with lighter values in the core of the dolomite body (Fig. 7).

Strontium isotopes

The two limestone samples have $^{87}Sr/^{86}Sr$ ratios of 0.70786 and 0.70793, which is similar to the reported values for Precambrian Khufai Formation carbonate, i.e. 0.7078 to 0.7085 (Burns et al., 1994; Le Guerroue et al., 2006b). The $^{87}Sr/^{86}Sr$ ratios of the fine-crystalline dolomite vary from 0.70934 to 0.71006 and those of the coarse-crystalline dolomite range from 0.70919 to 0.70973 (with one outlier at 0.71146). Excluding this one outlier, a statistical analysis of the z distribution shows that the $^{87}Sr/^{86}Sr$ ratio in fine-crystalline dolomite is significantly higher than that in coarse-crystalline dolomite (at >99% confidence level). Both fine and coarse-crystalline dolomites are strongly enriched in ^{87}Sr compared to the limestone. The $^{87}Sr/^{86}Sr$ values of the dolomite form a cluster and there is no correlation with $\delta^{13}C$ and $\delta^{18}O$ (Fig. 9). The variation of the $^{87}Sr/^{86}Sr$ ratio was also assessed along one of the transects, but there is no clear trend.

Temperature and composition of dolomitizing fluids

Fluid inclusions in both dolomite and calcite (present as cement in vugs in dolomite) are all two-phase aqueous fluid inclusions. No petroleum inclusions were observed (as confirmed by fluorescence microscopy). The inclusions are mostly 2 by 3 µm in size in dolomite and up to 8 by 10 µm in calcite. Fluid inclusion petrography was carried out and a primary origin of the fluid inclusions was interpreted based on the cloudy core and clear rim of the dolomite crystals and the small size (<5 µm) of the inclusions (Goldstein and Reynolds, 1994). Still, since the density of the fluid inclusion distribution does not vary with growth zonations (except for the rim), the main bulk of the dolomite crystals is totally cloudy and the interpreted primary origin of the inclusions may be ambiguous. Secondary trails of fluid inclusions were avoided, since our aim was to reconstruct the dolomite formation conditions, and thus we focused on fluid inclusions of primary origin. No clear changes in vapor to liquid ratio were observed within or between measured fluid inclusion assemblages. The variation in temperatures measured in inclusions of the same fluid inclusion assemblage is large. Due to the small size of the inclusions and poor visibility in dolomite, first melting of ice was not recognized in the dolomite wafers. First melting of ice and complete dissociation of hydrohalite was observed between -29 and -21ºC as eutectic temperature in inclusions within calcite (with one outlier inclusion at -51ºC), indicating the presence of mainly NaCl, and possibly some $CaCl_2$ or KCl dissolved in the fluid (Goldstein and Reynolds, 1994). The average value for the homogenization temperature measured in fluid inclusions of five fluid inclusion assemblages in white dolomite varies from 129 to 143ºC (with one standard deviation σ ranging between 10 and 20; Fig. 10A). In pore-filling calcite cement, the average homogenization temperature is higher, i.e. 169ºC ($\sigma = 17$; Fig. 10B). The average salinity, derived from the final melting temperature of ice using the equation from Bodnar (1993), is higher in dolomite (22 wt% NaCl eq, $\sigma = 4$; Fig. 10B) than in calcite (16 wt% NaCl eq, $\sigma = 5$; Fig. 10B). There is no correlation between the homogenization temperature and the temperature of final melting of ice in the inclusions; inclusions with similar homogenization temperature show a wide range in salinity (Fig. 10C). Neither is there a correlation between fluid inclusion size and homogenization temperature or salinity.

Also clumped isotopes have been used to constrain the dolomite formation temperature. The average $\Delta 47$ value per sample falls between 0.349 and 0.378 for four dolomite samples measured (Table 2). These values correspond to a temperature between 233 and 289ºC (average of 262ºC) based on the calibration of Passey and Henkes (2012). These temperatures are thus much higher than the fluid inclusion homogenization temperature.

DISCUSSION

Dimension of dolomite geobodies

Structurally-controlled dolomite bodies globally can vary significantly in size (Table 1). Based on the reported examples, it is clear that the dimension and shape of this type of dolomite body is determined by the associated fault or fracture distribution (Table 1). The bodies have an elongated shape following the fault/fracture trend and, at least in this study, there is no correlation between length and width of the dolomite bodies. The tectonic framework that generated the fracture network plays an essential role in the distribution of the dolomite bodies. Dolomitization has been reported in both compressional and extensional regimes. However, a link with transtensional faults seems to prevail (Davies and Smith, 2006).

The width of the structurally-controlled dolomite bodies, i.e. the extent of dolomitization away from the fault/fracture, is determined by the host rock properties at the time of dolomitization. The meter-scale width of dolomite bodies in Precambrian host rock (this study) and Jurassic host rock in northern Oman (Vandeginste et al., 2013b) is probably related to the tight nature of the limestone under deep burial conditions at the time of dolomitization, but could also be linked to a limited source and/or fluid flow driving mechanism for dolomitizing fluids. In contrast, dolomite bodies of kilometer-scale width have been reported in Oligocene-Miocene host rock in Borneo, where the limestone must have been highly permeable at the time of dolomitization (Wilson et al., 2007). As reported previously for such large bodies, the extent of dolomitization is not equal on both sides of the faults, but dolomitization occurs preferentially on the downthrown side or hanging wall of extensional faults (Black et al., 1981; Davies and Smith, 2006).

Origin of dolomitizing fluids

Circulation of late-diagenetic fluids along fractures resulted in abundant fracture-related red (weathering color) dolomite bodies in the Khufai Formation. The geochemical signature of the late-diagenetic dolomite is significantly different from that of the limestone, both in terms of element and stable isotope composition. The presence of saddle dolomite, and the high Fe (up to 4.4 wt%) and Mn (up to 0.8 wt%) contents in dolomite suggest formation by burial fluids that interacted with a non-carbonate source. Similarly, the elevated $^{87}Sr/^{86}Sr$ ratio in dolomite (0.7092-0.7101) compared to the ratio in the Khufai limestone (0.7079) suggests fluid interaction with a source of radiogenic strontium, for instance basement or Precambrian siliciclastic beds. The Precambrian basement has high $^{87}Sr/^{86}Sr$ values of up to 0.774 (Gass et al., 1990). The feldspathic sandstone of the Masirah Bay Formation (underlying the

Khufai Formation) is a more likely source, since these beds were aquifers and radiogenic strontium was leached from the feldspars.

Also fluid inclusions could potentially provide more information on the nature of the dolomitizing fluids. However, the large ranges in homogenization temperature as well as salinity suggests that the inclusion may have been altered by some degree of leaking, refilling or stretching. The rocks have undergone deep burial with temperatures of about 250ºC or more (Saddiqi et al., 2006) and it is thus expected that fluid inclusion properties would change due to stretching or leaking during overheating (Burruss, 1987; Prezbindowski, 1987) or alteration, potentially refilling during subsequent tectonic events. It is difficult to pinpoint the exact cause for the large range in the data because of the lack of correlation between homogenization temperature, salinity and vapour to gas ratio in the inclusions, but post-Cretaceous refilling of the fluid inclusions seems most likely. The temperature derived from the clumped isotopes is significantly higher than that of the fluid inclusions (even if a pressure correction was applied to the fluid inclusions). We interpret the clumped isotope data to reflect an apparent equilibrium temperature sensu Passey and Henkes (2012) that was obtained during uplift after clumped isotope reordering during deep burial. Thus, neither the fluid inclusion homogenization temperature nor the clumped isotope derived temperature is interpreted to reflect the temperature of dolomite formation. If we reconstruct the $\delta^{18}O$ of the dolomitizing fluid using the $\delta^{18}O$ of the dolomite, the temperature obtained from both fluid inclusions and clumped isotopes, and the equation of Land (1985), then a $\delta^{18}O_{fluid}$ of +5 to +7‰ VSMOW is obtained based on clumped isotope temperature and a $\delta^{18}O_{fluid}$ of -2 to 0‰ VSMOW is calculated using the fluid inclusion homogenization temperature (Fig. 11). Both $\delta^{18}O_{fluid}$ ranges are higher than that of early Ediacaran seawater, i.e. -5 to -7.5‰

VSMOW derived from a $\delta^{18}O$ value of -7.5 to -10‰ VPDB for early Ediacaran marine calcite (Shields and Veizer, 2002) precipitated at 25ºC using the equation from Kim and O'Neil (1997). This would be consistent with an evaporated seawater origin. Because of the large difference (about 11‰) between Ediacaran seawater and the reconstructed $\delta^{18}O_{fluid}$ based on clumped isotope data, the Late Cretaceous deep burial and heating of the rocks and thus high likelihood of resetting of the clumped isotope signature, we think that the clumped isotope temperature is much higher than the dolomite formation temperature. In contrast, the fluid inclusion homogenization temperature probably approximates the dolomite formation temperature better, especially since this temperature is also closer to reported values for structurally-controlled dolomite formation (Davies and Smith, 2006).

Although the preservation of a pristine $\delta^{18}O$ signature in dolomite may be questioned based on the evidence of high-temperature deformation (cleavage twinning), evidence from CL petrography did not suggest dolomite recrystallization (no mottling observed). Moreover, dolomite that forms at depths of several hundreds to thousands of meters has been shown to be less prone to recrystallization since it generally forms as a stable phase (Machel, 2004). Hence, we interpret the measured $\delta^{18}O$ values in the fracture-related dolomite to represent the original dolomite signature from the time of dolomite formation. Moreover, using a common temperature for structurally-controlled dolomite formation, i.e. 150ºC (Davies and Smith, 2006) and the $\delta^{18}O$ measured in the dolomite, a reconstructed $\delta^{18}O$ of the dolomitizing fluid would give reasonable results for a subsurface brine in Ediacaran host rock, i.e. -1 to +1‰ VSMOW (Fig. 11). In contrast, the $\delta^{18}O$ values measured in limestone are interpreted to be reset (compared to the signature at the time of limestone deposition) due to recrystallization at high temperature during deep burial; they are about 5‰ more depleted than time-equivalent marine carbonates (Burns et al., 1994; Sawaki et al., 2010).

Textural and geochemical heterogeneity within dolomite geobodies

The transects across the structurally-controlled diagenetic geobodies show that zebra dolomite textures as well as subvertical coarse dolomite veins are common throughout the dolomite body. In contrast, calcite-filled vugs are most abundant at the rim of the bodies, probably indicating a greater degree of “overdolomitization” (Lucia and Major, 1994) in the core compared to the rims. A higher (pre-calcite cementation) porosity near the rim of the dolomite body is consistent with models and observations documented in Sharp et al. (2010) and Wilson et al. (2007). The zebra dolomite texture is variable with roughly evenly spaced bands, more irregular band thicknesses, and variation in orientation of the bands (including curved bands), but these are not constrained to particular zones across the body. A distinct texture comprised of white coarse dolomite surrounding floating grey fine dolomite “clasts”, similar to the breccia fabric close to faults described by Sharp et al. (2010), is predominant at the intersection of two fracture-related dolomite bodies. In general, dolomite bodies within these intersections also contain a greater abundance of white coarse dolomite.

The analysis of proxies shows that there is little or no geochemical variation across the dolomite bodies (Fig. 7). There is also no clear change in $\delta^{13}C$ (Fig. 7), $^{87}Sr/^{86}Sr$ and several elemental contents. In contrast, $\delta^{18}O$ is most negative in the core of the fracture-related dolomite body (Fig. 7), whereas Fe content (and also Mn content) is generally higher at the rims of the dolomite bodies (Fig. 7). Although the $\delta^{18}O$ signature of light-colored coarse dolomite is more negative (0.2‰ on average) than that of dark-colored fine dolomite in most instances where both phases were taken in the same hand sample, this is less consistent or significant than the trend observed along a transect through the dolomite bodies (with a depletion of 1 to 2‰ in the core compared to the rim of the dolomite body). This probably indicates that although the lighter-colored dolomite bands are probably younger than the darker-colored dolomite bands during zebra dolomite formation based on the youngest cement phase being in the center of the white bands (Nielsen et al., 1998), there is also a relative chronology in the formation of zebra dolomite within the dolomite body. Hereby, the center of the dolomite body probably formed at the highest temperature derived from the most negative oxygen isotope signature, which may relate to the proximity of the dominant fluid flow pathway and potentially slow heating of the system and gradual decrease in Fe content. Alternatively, the dolomitizing fluids may have been focused simultaneously through several parallel fractures, since some smaller dolomite zones (or thick veins) are separated from the main fracture-related dolomite body by wedges of host rock limestone. However, veins or fractures do not need to occur simultaneously, as the core of the body could be cemented and, thus, diverging the flow of dolomitizing fluid to the sides of the main body.

Timing and tectonic context of the fracture-related dolomitization event

The Precambrian rocks in Jebel Akhdar have undergone a long burial history (Fig. 12) comprising several tectonic events, including a moderate compressive phase of late Panafrican tectonism, the Hercynian Orogeny in the Carboniferous (Faqira et al., 2009; Mann and Hanna, 1990), the Alpine Orogeny with Semail Ophiolite obduction in Late Cretaceous, and the Zagros compression in Miocene to Pliocene. The impact of the multiple tectonic events on the rocks is clearly testified by the deformed, folded and fractured, nature of the rocks studied. The dolomitizing fluids clearly exploited fractures, since the dolomite geobodies crosscut beds. Both the fractures and the trigger for dolomitizing fluid flow are most likely linked to a tectonic event. However, given the multiple tectonic events that affected the rocks, assigning an approximate absolute age to the dolomitization event is very challenging.

Cross-cutting relationships demonstrate that the fracture-related dolomite formed in between the onset and termination of bedding-parallel stylolitization. This indicates that the dolomite predates the Alpine Orogeny; it predates Campanian time, when the rocks were at their deepest burial due to the Semail ophiolite obduction. Moreover, the curved nature of the dolomite geobodies suggests that some folding, related to the Alpine Orogeny, occurred after the dolomitization event. The structural orientation of the dolomite geobodies suggests dolomitizing fluids were channeled through a fracture network that formed under a vertical compressional stress, interpreted to relate to burial overburden pressure, as well as a NNE horizontal compressional stress. The fracture network that the dolomitizing fluids exploited is probably linked to a pre-Permian folding event, since this type of dolomite is not found in post-Carboniferous layers and because the folding that characterizes the pre-Permian sequence is not seen in post-Carboniferous layers. The Khufai Formation is a limestone layer that sits in between much thicker siliciclastic layers, which exhibit well developed cleavage. The difference in lithologies and their response to horizontal compressional stress can have led to the large scale folding of the formations and more brittle deformation in the limestone bed. The most probable tectonic compressional event that caused folding of the pre-Permian strata is the Hercynian Orogeny in the Carboniferous (Mann and Hanna, 1990). We propose that the dolomite geobodies present in the Khufai Formation host rock formed through hot dolomitizing fluids that exploited tectonic fractures during the Hercynian Orogeny. The orientation of the dolomite geobodies is similar to the N-trending Hercynian grain (Ziegler, 2001) and could also be influenced by an inheritance of structures that developed during the Amar collision (640-620 Ma) of the Rayn Plate in the east with the Arabian-Nubian Craton in the west, and the ensuing Najd Rift (570-530 Ma) (Al-Husseini, 2000).

CONCLUSION AND IMPLICATIONS

By definition, it can be expected that the dimension of structurally-controlled dolomite geobodies is mainly controlled by the distribution and 3D geometry of faults or fractures. Thus, the longest extent of the dolomite geobody follows the dominant fracture direction. Hence, understanding the facture network and the conductivity of the fracture network at the time of dolomitization is key in predicting the distribution of this type of dolomite geobodies when looking at subsurface examples. The width of these geobodies can vary significantly, up to kilometer-scale in permeable host rocks as documented in other studies, and up to meter-scale (or tens of meters) in tighter host rocks as demonstrated here. The host rock permeability plays a key role in the extent of dolomitization away from the fault/fracture. Therefore, it is essential to characterize all diagenetic products that affected the host rock, and thus, to have a clear insight into the timing of dolomitization and the characteristics of the host rock at that time. Predictive rules for the dolomite body width cannot be derived from host rock permeability alone, since additional factors, such as fluid source reservoir, fluid flow rate, characteristics of fault activity (pressure drop conditions and number of episodic cycles), etc. play a role as well. Specific studies where this information can be reconstructed could make a significant contribution in this respect.

Geochemical proxies have been applied in this study to gain information on the dolomite formation conditions, i.e. origin of dolomitizing fluids, structural setting, estimated timing. The data suggest that the dolomite hosted in the Ediacaran Khufai Formation host rock formed by fluids that interacted with siliciclastic formations (most likely the Masirah Bay feldspathic sandstones) probably during the Hercynian Orogeny (or pre-Permian time). Both fluid inclusion and clumped isotope data are interpreted to be inconclusive with respect to the dolomite formation temperature.

Heterogeneity with respect to textures and petrophysical properties can be significant in large fracture-related dolomite bodies (kilometer-scale long and wide), as reported in previous studies. However, as the results from the current study indicate, there is only minor heterogeneity in texture and geochemical signature within small dolomite geobodies (hundreds of meters long and meters to tens of meters wide). This result has important implications for subsurface applications: the interaction between connected vuggy porosity (especially present at the rims of the dolomite body) and remnant fracture porosity could greatly impact permeability along the axis of the fault. Thus, care should be taken when characterizing small-scale dolomite geobodies as they may not always be considered as homogeneous for modeling purposes, but should be documented as diagenetic geobodies with petrophysical characteristics different from the host rock.

ACKNOWLEDGEMENTS

This research project is funded by Qatar Petroleum, Shell and the Qatar Science and Technology Park (QSTP). Field logistic was provided by the Shuram company. We would like to thank Manuela Stehle for assistance during field work and Martin Gill (XRD), Emma Williams and Stanislav Strekopytov (ICP-AES), Claude Merlet and Bernard Boyer (microprobe) and Simon Davis (stable isotopes) for their help with various analytical techniques. The authors are grateful for the helpful comments by the AAPG editor Michael Sweet, reviewer Jeff Lonnee and an anonymous reviewer.

FIGURE CAPTIONS

Fig. 1. Geological setting of the study area. (A) Geological map of northern Oman, simplified after Béchennec et al. (1993). (B) More detailed geological map of the Jebel Akhdar tectonic window, modified after Béchennec et al. (1993). (C) Nomenclature of the Precambrian Huqf Supergroup in Jebel Akhdar, modified after Allen (2007). This synthesis of nomenclature was based on previous work from Allen et al. (2004), Glennie et al. (1974), Kapp and Llewellyn (1965), Leather (2001), Leather et al. (2002), McCarron (2000), Rabu et al. (1986). (D) Google Earth satellite image of study area with indication of sampled sections, i.e. BAB and BAC on mountain flank on southern side of Snake Canyon (N23º12’26”, E57º23’21”), BAD, BAE, BAF and BAG on mountain flank on northern side of Snake Canyon (N23º12’38”, E57º23’26”) and BAH close to entrance of Snake Canyon (N23º12’32”, E57º23’11”).

Fig. 2. Photographs of outcrops in Khufai Formation and polished and stained hand samples. (A) Reddish weathered fracture-related dolomite bodies in black Khufai Formation host rock on the mountain flank at the north side of the valley (at main sampling site). (B) Reddish weathered dolomite body cross-cutting steep beds of Khufai Formation at northern sampling site in Wadi Bani Awf. (C) Small dolomite body with parts that are both parallel and perpendicular to bedding (northern sampling site). (D) Curved reddish weathered dolomite bodies cross-cutting stratigraphic beds.

(E) Polished and stained hand sample of zebra dolomite (coin of 2.25 cm diameter as scale). (F) Zebra dolomite with bedding parallel bands and subvertical veins (15 cm long ballpoint as scale). (G) Polished and stained hand sample showing calcite cement in vugs in dolomite (coin of 2.25 cm diameter as scale). (H) Red dolomite along bedding parallel stylolites and in veins perpendicular to bedding (lens cap of 5.8 cm diameter as scale).

Fig. 3. Rose diagrams. (A) Fracture-related dolomite bodies derived from Google Earth satellite images. (B) Fractures along BAC section on outcrop (mountain flank on southern side of the valley). (C) Fractures along BAG section on outcrop (mountain flank on northern side of the valley). The number of measurements is indicated by “n” at the left bottom of each diagram. The predominant trend is NNE-SSW to NE-SW.

Fig. 4. Dimensions of mapped discontinuous (at surface) dolomite geobodies measured on Google Earth satellite images. (A) Cross plot of length versus width. Correlation coefficient is 0.1. (B) Histogram of length. (C) Histogram of width.

Fig. 5. Photomicrographs of thin sections. Scale bar is 500 µm. (A) Stained thin section of recrystallized peloidal limestone that is crosscut by a bedding parallel stylolite and later (post-stylolitization) calcite veins. (B) Dolomite that is crosscut by bedding parallel stylolite. (C) Dolomite with brownish alteration band. (D) Cathodoluminescence microscope view of C showing yellowish luminescence along altered band and zonation pattern of overlying dolomite with some saddle dolomite crystals.

Fig. 6. Mg versus Fe cross plot of limestone and fracture-related dolomite samples.

Fig. 7. Overview of geochemical variation along 5 different transects (named BAB, BAC, BAE, BAG, BAH) for Fe content (left), $\delta^{13}C$ (middle) and $\delta^{18}O$ (right). Data are separated for limestone, fine dolomite, coarse dolomite or calcite cement. Distance is given in meters with positive value for samples at the right side of the fracture center and negative values for samples at the left side of the fracture center (facing the outcrop). Limestone along the transect is indicated by a shaded background on the plots. The weighted average fit curve for dolomite data is presented by a thick line.

Fig. 8. Stable carbon and oxygen isotope cross plot.

Fig. 9. Cross plot of Sr isotopic ratios versus stable oxygen isotope values for limestone, and fine and coarse dolomite zones.

Fig. 10. Fluid inclusion data in fracture-related dolomite and pore-filling calcite cement. (A) Histogram of homogenization temperature. (B) Histogram of salinity derived from final melting temperature of ice. (C) Homogenization versus salinity data presented for fluid inclusions in fluid inclusion assemblages (FIA) in dolomite (Dol) and calcite (Cc).

Fig. 11. Graphical representation of the oxygen isotopic equilibrium between dolomite, fluid (on SMOW scale) and temperature (Land, 1985). The $\delta^{18}O_{dolomite}$ (on VPDB scale) is represented versus temperature, i.e. temperature derived from

clumped isotopes based on Passey and Henkes (2012) calibration and homogenization temperature from fluid inclusion measurements. The error bars represent standard error for the clumped isotope measurements and standard deviation for the fluid inclusion measurements.

Fig. 12. Reconstructed burial curve for the Precambrian Khufai Formation outcrop in Wadi Bani Awf. The age of the Precambrian Khufai Formation is based on Allen (2007). The burial curve is based on Visser (1991) for the Precambrian, Le Nindre et al. (2003) for Permian through earliest Late Cretaceous time (curve read on depth scale) and two interpretations from Mount et al. (1998) and Saddiqi et al. (2006) for the uplift history (curve read on temperature scale). Cambrian to Carboniferous burial for the study area is not well constrained since deposits of this time interval are missing in Jebel Akhdar.

TABLES

Table 1. Selected examples of dimensions of structurally-controlled dolomite bodies (Black et al., 1981; Boni et al., 2000; Braithwaite and Rizzi, 1997; Davies and Smith, 2006; Lavoie et al., 2010; Lopez-Horgue et al., 2010; Shah et al., 2012; Sharp et al., 2010; Vandeginste et al., 2013b; Wierzbicki et al., 2006; Wilson et al., 2007).

Table 2. Clumped isotope data of replicates of 4 dolomite samples. Sample $\Delta47$ and temperature present the average value ± standard error. The temperature is based on the calibration of Passey and Henkes (2012).

REFERENCES

Al-Husseini, M. I., 2000, Origin of the Arabian Plate structures: Amar Collision and Najd Rift: GeoArabia, v. 5, p. 527-542.

Allen, P. A., 2007, The huqf supergroup of Oman: Basin development and context for neoproterozoic glaciation: Earth-Science Reviews, v. 84, p. 139-185.

Allen, P. A., J. Leather, and M. D. Brasier, 2004, The Neoproterozoic Fiq glaciation and its aftermath, Huqf supergroup of Oman: Basin Research, v. 16, p. 507-534.

Béchennec, F., J. Le Métour, J. P. Platel, and J. Roger, 1993, Geological map of the Sultanate of Oman: Ministry of Petroleum and Minerals.

Black, D. F. B., W. C. J. MacQuown, and R. J. DeHaas, 1981, The relation of dolomite associated with faults to the stratigraphy and structure of Central Kentucky: United States Government Printing Office, Washington, Geological Survey Professional Paper 1151-A.

Bodnar, R. J., 1993, REVISED EQUATION AND TABLE FOR DETERMINING THE FREEZING-POINT DEPRESSION OF H2O-NACL SOLUTIONS: Geochimica Et Cosmochimica Acta, v. 57, p. 683-684.

Boni, M., G. Parente, T. Bechstädt, B. De Vivo, and A. Iannace, 2000, Hydrothermal dolomites in SW Sardinia (Italy): evidence for a widespread late-Variscan fluid flow event: Sedimentary Geology, v. 131, p. 181-200.

Boudier, F., J. L. Bouchez, A. Nicolas, M. Cannat, G. Ceuleneer, M. Misseri, and R. Montigny, 1985, Kinematics of oceanic thrusting in the Oman ophiolite - model of plate convergence: Earth and Planetary Science Letters, v. 75, p. 215-222.

Braithwaite, C. J. R., and G. Rizzi, 1997, The geometry and petrogenesis of hydrothermal dolomites at Navan, Ireland: Sedimentology, v. 44, p. 421-440.

Breton, J. P., F. Béchennec, J. Le Métour, L. Moen-Maurel, and P. Razin, 2004, Eoalpine (Cretaceous) evolution of the Oman Tethyan continental margin: insights from a structural field study in Jabal Akhdar (Oman Mountains): GeoArabia, v. 9, p. 41-57.

Burns, S. J., U. Haudenschild, and A. Matter, 1994, The strontium isotopic composition of carbonates from the late Precambrian (approximate-to-560-540 Ma) Huqf Group of Oman: Chemical Geology, v. 111, p. 269-282.

Burruss, R. C., 1987, DIAGENETIC PALEOTEMPERATURES FROM AQUEOUS FLUID INCLUSIONS - RE-EQUILIBRATION OF INCLUSIONS IN CARBONATE CEMENTS BY BURIAL HEATING: Mineralogical Magazine, v. 51, p. 477-481.

Davies, G. R., and L. B. Smith, Jr., 2006, Structurally controlled hydrothermal dolomite reservoir facies: An overview: AAPG Bulletin, v. 90, p. 1641-1690.

Dennis, K. J., H. P. Affek, B. H. Passey, D. P. Schrag, and J. M. Eiler, 2011, Defining an absolute reference frame for 'clumped' isotope studies of CO2: Geochimica Et Cosmochimica Acta, v. 75, p. 7117-7131.

Dewit, J., M. Huysmans, P. Muchez, D. W. Hunt, J. B. Thurmond, J. Verges, E. Saura, N. Fernandez, I. Romaire, P. Esestime, and R. Swennen, 2012, Reservoir characteristics of fault-controlled hydrothermal dolomite bodies: Ramales

Platform case study, *in* J. Garland, J. E. Neilson, S. E. Laubach, and K. J. Whidden, eds., Advances in Carbonate Exploration and Reservoir Analysis, v. 370: London, Geological Society, London, Special Publications.

Dickson, J. A. D., 1966, Carbonate identification and genesis as revealed by staining: Journal of Sedimentary Petrology, v. 36, p. 491-505.

Faqira, M., M. Rademakers, and A. M. Afifi, 2009, New insights into the Hercynian Orogeny, and their implications for the Paleozoic Hydrocarbon System in the Arabian Plate: Geoarabia, v. 14, p. 199-228.

Gass, I. G., A. C. Ries, R. M. Shackleton, and J. D. Smewing, 1990, Tectonics, geochronology and geochemistry of the Precambrian rocks of Oman: Geology and Tectonics of the Oman Region, v. 49, 585-599 p.

Genna, A., P. Nehlig, E. Le Goff, C. Guerrot, and M. Shanti, 2002, Proterozoic tectonism of the Arabian Shield: Precambrian Research, v. 117, p. 21-40.

Glennie, K. W., M. G. A. Boef, M. W. Hughes-Clarke, M. NMoody-Stuart, W. F. H. Pilaar, and B. M. Reinhart, 1974, Geology of the Oman Mountains: Koninkl. Ned. Geol. Mijnbouwk. Gen. Verh., v. 31, p. 423 pp.

Goldstein, R. H., and T. J. Reynolds, 1994, Systematics of fluid inclusions in diagenetic minerals: SEPM Short Course Notes, v. 31, 188 p.

Hacker, B. R., 1994, Rapid emplacement of young oceanic lithosphere - Argon geochronology of the Oman ophiolite: Science, v. 265, p. 1563-1565.

Harris, P. M., S. J. Purkis, and J. Ellis, 2011, Analyzing spatial patterns in modern carbonate sand bodies from Great Bahama Bank: Journal of Sedimentary Research, v. 81, p. 185-206.

Kapp, H. E., and P. G. Llewellyn, 1965, The geology of the Central Oman Mountains, Report S00005-9, Geological Group, Petroleum Development Oman.

Kim, S.-T., A. Mucci, and B. E. Taylor, 2007, Phosphoric acid fractionation factors for calcite and aragonite between 25 and 75 degrees C: Revisited: Chemical Geology, v. 246, p. 135-146.

Kim, S.-T., and J. R. O'Neil, 1997, Equilibrium and nonequilibrium oxygen isotope effects in synthetic carbonates: Geochimica Et Cosmochimica Acta, v. 61, p. 3461-3475.

Land, L. S., 1985, The origin of massive dolomite: Journal of Geological Education, v. 33, p. 112-125.

Lapponi, F., G. Casini, I. Sharp, W. Blendinger, N. Fernandez, I. Romaire, and D. Hunt, 2011, From outcrop to 3D modelling: a case study of a dolomitized carbonate reservoir, Zagros Mountains, Iran: Petroleum Geoscience, v. 17, p. 283-307.

Lavoie, D., G. Chi, M. Urbatsch, and W. J. Davis, 2010, Massive dolomitization of a pinnacle reef in the Lower Devonian West Point Formation (Gaspe Peninsula, Quebec): An extreme case of hydrothermal dolomitization through fault-focused circulation of magmatic fluids: AAPG Bulletin, v. 94, p. 513-531.

Le Guerroue, E., P. A. Allen, and A. Cozzi, 2006a, Chemostratigraphic and sedimentological framework of the largest negative carbon isotopic excursion in Earth history: The Neoproterozoic Shuram Formation (Nafun Group, Oman): Precambrian Research, v. 146, p. 68-92.

Le Guerroue, E., P. A. Allen, A. Cozzi, J. L. Etienne, and M. Fanning, 2006b, 50 Myr recovery from the largest negative delta C-13 excursion in the Ediacaran ocean: Terra Nova, v. 18, p. 147-153.

Le Nindre, Y. M., D. Vaslet, J. Le Metour, J. Bertrand, and M. Halawani, 2003, Subsidence modelling of the Arabian platform from permian to paleogene outcrops: Sedimentary Geology, v. 156, p. 263-285.

Leather, J., 2001, Sedimentology, chemostratigraphy and geochronology of the lower Huqf Supergroup, Oman, Trinity College Dublin, Ireland, 227 p.

Leather, J., P. A. Allen, M. D. Brasier, and A. Cozzi, 2002, Neoproterozoic snowball Earth under scrutinity: evidence from the Fiq glaciation of Oman: Geology, v. 30, p. 891-894.

Lopez-Horgue, M. A., E. Iriarte, S. Schroeder, P. A. Fernandez-Mendiola, B. Caline, H. Corneyllie, J. Fremont, M. Sudrie, and S. Zerti, 2010, Structurally controlled hydrothermal dolomites in Albian carbonates of the Ason valley, Basque Cantabrian Basin, Northern Spain: Marine and Petroleum Geology, v. 27, p. 1069-1092.

Lucia, F. J., and R. P. Major, 1994, Porosity evolution through hypersaline reflux dolomitization, *in* B. H. Purser, M. E. Tucker, and D. H. Zenger, eds., Dolomites: A Volume in Honour of Dolomieu, v. 21, International Association of Sedimentologists, Special Publications, p. 325-341.

Lunt, I. A., G. H. S. Smith, J. L. Best, P. J. Ashworth, S. N. Lane, and C. J. Simpson, 2013, Deposits of the sandy braided South Saskatchewan River: Implications for the use of modern analogs in reconstructing channel dimensions in reservoir characterization: Aapg Bulletin, v. 97, p. 553-576.

Machel, H. G., 2004, Concepts and models of dolomitization: a critical reappraisal, *in* C. J. R. Braithwaite, G. Rizzi, and G. Darke, eds., The geometry and petrogenesis of dolomite hydrocarbon reservoirs: Geological Society, London, Special Publications, v. 235: London, The Geological Society of London, p. 7-63.

Mann, A., and S. S. Hanna, 1990, The tectonic evolution of pre-Permian rocks, Central and Southeastern Oman Mountains, *in* A. H. F. Robertson, M. P. Searle, and A. C. Ries, eds., The Geology and Tectonics of the Oman Region, v. 49: London, Geological Society Special Publication, p. 307-325.

McCarron, G. M. E., 2000, The sedimentology and chemostratigraphy of the Nafun Group, Huqf Supergroup, Oman, University of Oxford, 175 p.

Merlet, C., 1994, An accurate computer correction program for quantitative electron probe microanalysis: Mikrochimica Acta, v. 114/115, p. 363-376.

Mount, V. S., R. I. S. Crawford, and S. C. Bergman, 1998, Regional structural style of the central and southern Oman Mountains: Jebel Akhdar, Saih Hatat, and the Northern Ghaba Basin: GeoArabia, v. 3, p. 475-490.

Nielsen, P., R. Swennen, P. H. Muchez, and E. Keppens, 1998, Origin of Dinantian zebra dolomites south of the Brabant-Wales Massif, Belgium: Sedimentology, v. 45, p. 727-743.

Passey, B. H., and G. A. Henkes, 2012, Carbonate clumped isotope bond reordering and geospeedometry: Earth and Planetary Science Letters, v. 351, p. 223-236.

Poupeau, G., O. Saddiqi, A. Michard, B. Goffe, and R. Oberhansli, 1998, Late thermal evolution of the Oman Mountains subophiolitic windows: Apatite fission-track thermochronology: Geology, v. 26, p. 1139-1142.

Pranter, M. J., R. D. Cole, H. Panjaitan, and N. K. Sommer, 2009, Sandstone-body dimensions in a lower coastal-plain depositional setting: Lower Williams Fork Formation, Coal Canyon, Piceance Basin, Colorado: Aapg Bulletin, v. 93, p. 1379-1401.

Prezbindowski, D. R., 1987, EXPERIMENTAL STRETCHING OF FLUID INCLUSIONS IN CALCITE - IMPLICATIONS FOR DIAGENETIC STUDIES: Geology, v. 15, p. 333-336.

Rabu, D., F. Béchennec, M. Beurrier, and G. Hutin, 1986, Geological Map of Nakhl: Sheet NF 40-3E, Explanatory Notes: Bureau de Recherches Géologiques et Minières, Orléans, France.

Rosenbaum, J., and S. M. F. Sheppard, 1986, An isotopic study of siderites, dolomites and ankerites at high temperatures: Geochimica Et Cosmochimica Acta, v. 50, p. 1147-1150.

Saddiqi, O., A. Michard, B. Goffe, G. Poupeau, and R. Oberhaensli, 2006, Fission-track thermochronology of the Oman Mountains continental windows, and current problems of tectonic interpretation: Bulletin De La Societe Geologique De France, v. 177, p. 127-143.

Sawaki, Y., T. Kawai, T. Shibuya, M. Tahata, S. Omori, T. Komiya, N. Yoshida, T. Hirata, T. Ohno, B. F. Windley, and S. Maruyama, 2010, Sr-87/Sr-86 chemostratigraphy of Neoproterozoic Dalradian carbonates below the Port Askaig Glaciogenic Formation, Scotland: Precambrian Research, v. 179, p. 150-164.

Shah, M. M., F. H. Nader, J. Dewit, R. Swennen, and D. Garcia, 2010, Fault-related hydrothermal dolomites in Cretaceous carbonates (Cantabria, northern Spain): Results of petrographic, geochemical and petrophysical studies: Bulletin De La Societe Geologique De France, v. 181, p. 391-407.

Shah, M. M., F. H. Nader, D. Garcia, R. Swennen, and R. Ellam, 2012, Hydrothermal Dolomites in the Early Albian (Cretaceous) Platform Carbonates (NW Spain): Nature and Origin of Dolomites and Dolomitising Fluids: Oil & Gas Science and Technology-Revue D Ifp Energies Nouvelles, v. 67, p. 97-122.

Sharp, I., P. Gillespie, D. Morsalnezhad, C. Taberner, R. Karpuz, J. Verges, A. Horbury, N. Pickard, J. Garland, and D. Hunt, 2010, Stratigraphic architecture and fracture-controlled dolomitization of the Cretaceous Khami and Bangestan groups: an outcrop case study, Zagros Mountains, Iran, *in* F. S. P. Van Buchem, K. D. Gerdes, and M. Esteban, eds., Mesozoic and Cenozoic Carbonate Systems of the Mediterranean and the Middle East: Stratigraphic and Diagenetic Reference Models: Geological Society Special Publication, v. 329, p. 343-396.

Shields, G., and J. Veizer, 2002, Precambrian marine carbonate isotope database: Version 1.1: Geochemistry Geophysics, Geosystems, v. 3, p. 10.1029/2001GC000266.

Vandeginste, V., C. M. John, and C. Manning, 2013a, Interplay between depositional facies, diagenesis and early fractures in the Early Cretaceous Habshan Formation, Jebel Madar, Oman: Marine and Petroleum Geology, v. 43, p. 489-503.

Vandeginste, V., C. M. John, T. van de Flierdt, and J. W. Cosgrove, 2013b, Linking process, dimension, texture and geochemistry in dolomite geobodies: a case study from Wadi Mistal (northern Oman): AAPG Bulletin, v. 97, p. 1181-1207.

Visser, W., 1991, Burial and thermal history of Proterozoic source rocks in Oman: Precambrian Research, v. 54, p. 15-36.

Wierzbicki, R., J. J. Dravis, I. Al-Aasm, and N. Harland, 2006, Burial dolomitization and dissolution of Upper Jurassic Abenaki platform carbonates, Deep Panuke reservoir, Nova Scotia, Canada: Aapg Bulletin, v. 90, p. 1843-1861.

Wilson, M. E. J., M. J. Evans, N. H. Oxtoby, D. S. Nas, T. Donnelly, and M. Thirlwall, 2007, Reservoir quality, textural evolution and origin of fault-associated dolomites: AAPG Bulletin, v. 91, p. 1247-1272.

Wright, V. P., A. C. Ries, and S. G. Munn, 1990, Intraplatformal basin-fill deposits from the Infracambrian Huqf Group, east Central Oman, *in* A. H. F. Robertson, M. P. Searle, and A. C. Ries, eds., The Geology and Tectonics of the Oman Region, v. 49: London, Geological Society Special Publication, p. 601-616.

Ziegler, M. A., 2001, Late Permian to Holocene paleofacies evolution of the Arabian Plate and its hydrocarbon occurrences: GeoArabia, v. 6, p. 445-504.

CURRICULUM VITAE OF THE AUTHORS

VEERLE VANDEGINSTE ~ *Dept. of Earth Science and Engineering, Imperial College London, SW7 2BP, London, UK; v.vandeginste@imperial.ac.uk*

Veerle Vandeginste is a research fellow with Imperial College London. She earned a PhD from KU Leuven (Belgium) in 2006. Veerle worked two years for the Geological Survey of Belgium, focusing on carbon capture and storage, and did a post-doc at CEREGE (France). Her research interests include carbonate diagenesis and sedimentology, stable isotope geochemistry, structural diagenesis and ore mineralization.

CÉDRIC M JOHN ~ *Dept. of Earth Science and Engineering, Imperial College London, SW7 2BP, London, UK; cedric.john@imperial.ac.uk*

Cédric John is a QCCSRC senior lecturer and head of the “Carbonate Research” group at Imperial College London. Cédric obtained his PhD from Potsdam University, did 2 years of post doc at UC Santa Cruz, and worked 3 years as a research scientist for the Integrated Ocean Drilling Program. His research focuses on carbonate sedimentology, diagenesis and clumped isotope palaeothermometry.

JOHN COSGROVE ~ *Dept. of Earth Science and Engineering, Imperial College London, SW7 2BP, London, UK; j.cosgrove@imperial.ac.uk*

John Cosgrove is professor of structural geology at Imperial College London. His research interests relate to the interplay between stress, fractures and fluid flow in the crust and its application to the movement of fluids through low permeability sediments and fractured rock masses.

CHRISTINA MANNING ~ *Dept. of Earth Sciences, Royal Holloway University of London, Egham, Surry TW20 0EX, UK; c.manning@es.rhul.ac.uk*

Christina Manning is a Post-Doctoral Research Officer at Royal Holloway University of London. She has extensive experience of a host of analytical techniques on a wide range of geological samples. She is the secretary of the Geochemistry Group and a member of EAG, EGU and GSA. Her current research interests include: measurement of diffusion profiles using laser ablation ICP-MS, reconstruction of petrogenetic histories from mineral cargoes, combined whole rock and mineral studies of ocean Island basalt to assess the formation and preservation of mantle heterogeneity.

Figure 1

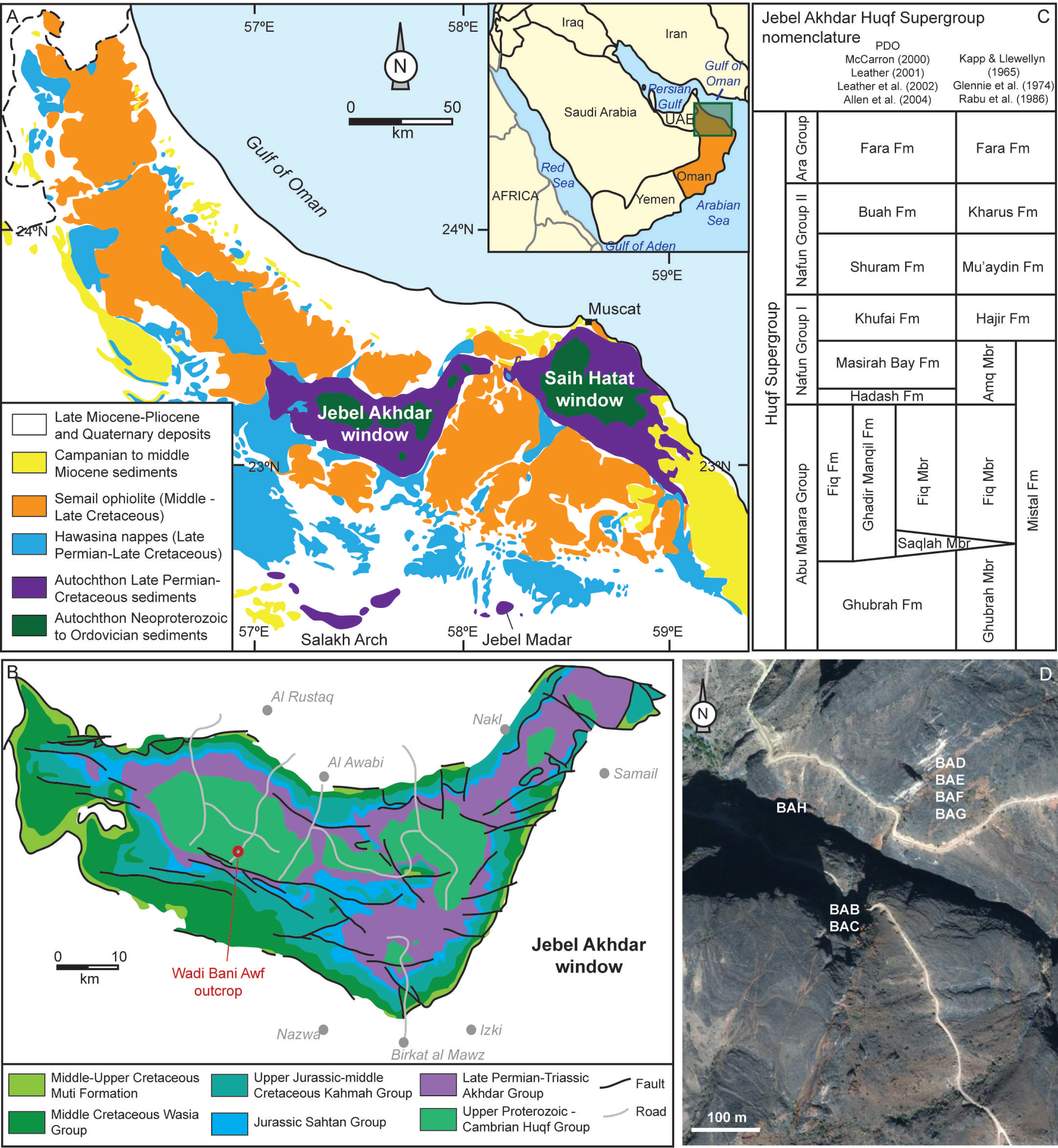
A
57ºE
58ºE
59ºE
24ºN
23ºN
N
0
50
km
Gulf of Oman
Iraq
Iran
Saudi Arabia
Persian Gulf
Gulf of Oman
UAE
Red Sea
AFRICA
Oman
Yemen
Arabian Sea
Gulf of Aden
Muscat
Saih Hatat window
Jebel Akhdar window
Salakh Arch
Jebel Madar
Late Miocene-Pliocene and Quaternary deposits
Campanian to middle Miocene sediments
Semail ophiolite (Middle - Late Cretaceous)
Hawasina nappes (Late Permian-Late Cretaceous)
Autochthon Late Permian-Cretaceous sediments
Autochthon Neoproterozoic to Ordovician sediments
C
Jebel Akhdar Huqf Supergroup nomenclature
PDO
McCarron (2000)
Leather (2001)
Leather et al. (2002)
Allen et al. (2004)
Kapp & Llewellyn (1965)
Glennie et al. (1974)
Rabu et al. (1986)
Huqf Supergroup
Ara Group
Nafun Group II
Nafun Group I
Abu Mahara Group
Fara Fm
Fara Fm
Buah Fm
Kharus Fm
Shuram Fm
Mu'aydin Fm
Khufai Fm
Hajir Fm
Masirah Bay Fm
Hadash Fm
Amq Mbr
Fiq Fm
Ghadir Manqil Fm
Fiq Mbr
Fiq Mbr
Mistal Fm
Saqlah Mbr
Ghubrah Fm
Ghubrah Mbr
B
Al Rustaq
Nakl
Al Awabi
Samail
Nazwa
Izki
Birkat al Mawz
0
10
km
Wadi Bani Awf outcrop
Jebel Akhdar window
Middle-Upper Cretaceous Muti Formation
Middle Cretaceous Wasia Group
Upper Jurassic-middle Cretaceous Kahmah Group
Jurassic Sahtan Group
Late Permian-Triassic Akhdar Group
Upper Proterozoic - Cambrian Huqf Group
Fault
Road
D
N
BAD
BAE
BAF
BAG
BAH
BAB
BAC
100 m

Figure 2

Figure 3


A
0
30
60
90
120
150
180
210
240
270
300
330
Google
Earth
n = 222
B
section
BAC
n = 95
C
section
BAG
n = 62

Figure 4

A
B
C
Dolomite body width (m)
Dolomite body length (m)
Frequency
Dolomite body length (m)
Frequency
Dolomite body width (m)

Figure 5

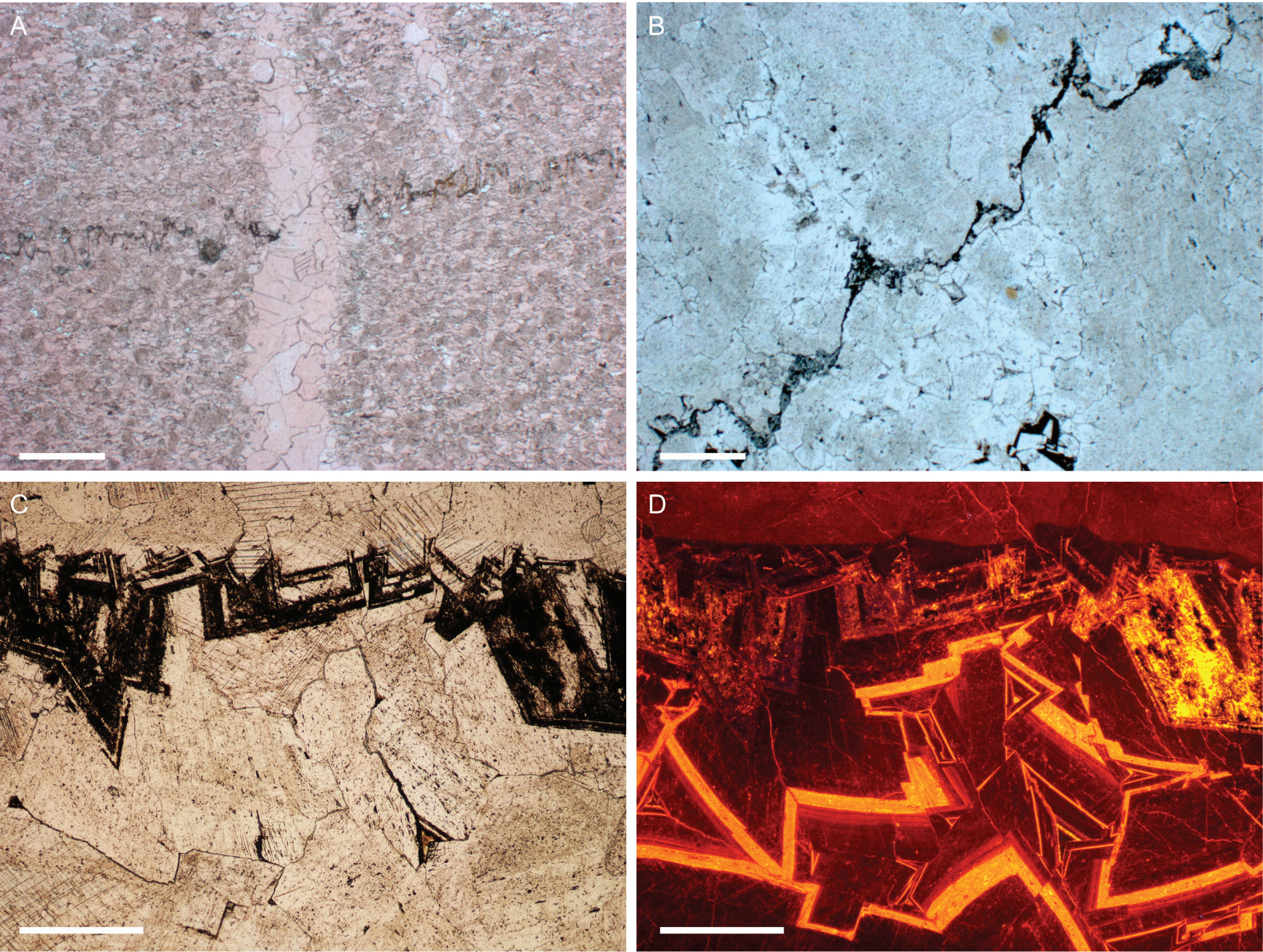

Figure 6

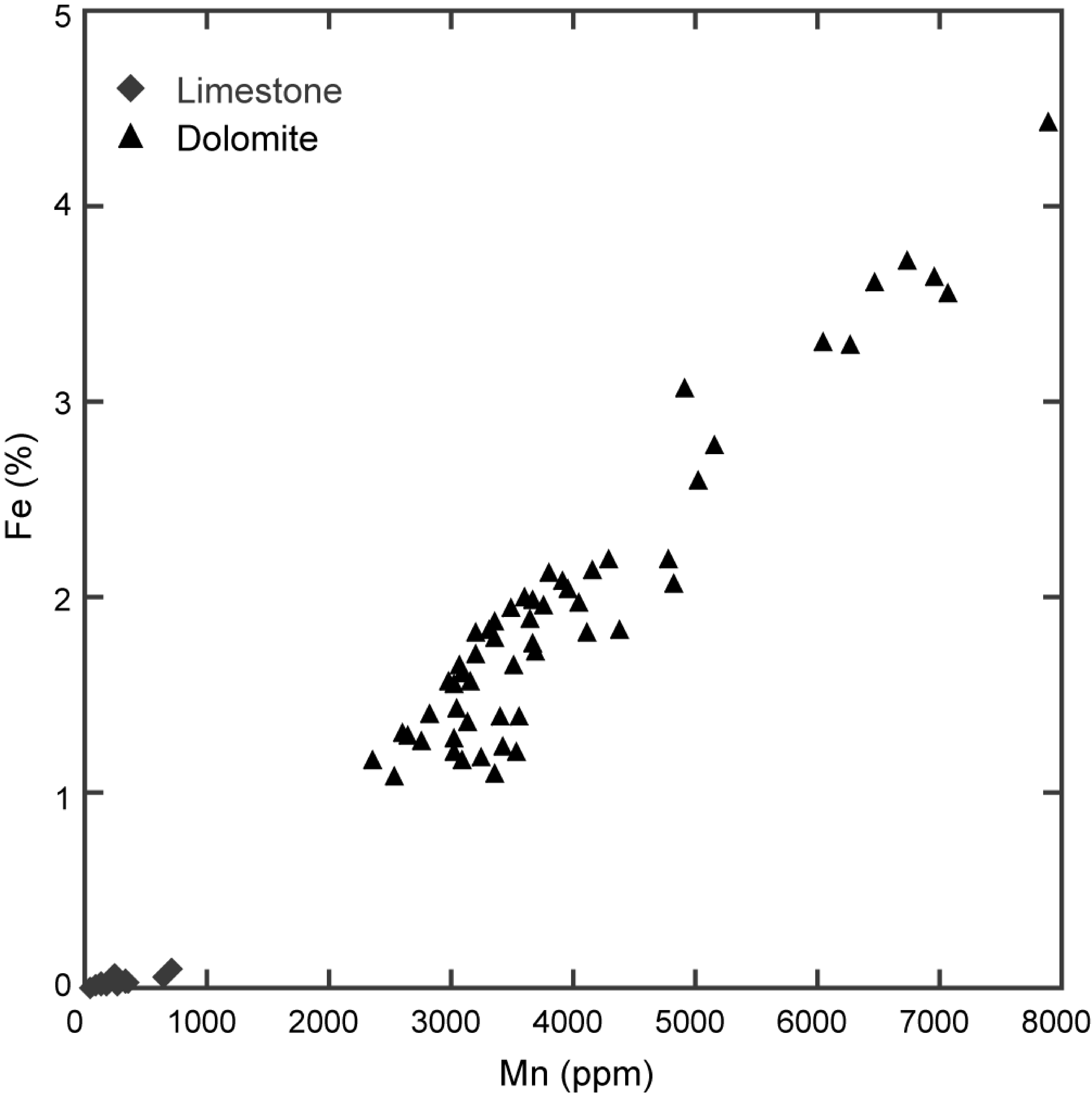
Limestone
Dolomite
Fe (%)
Mn (ppm)
0
1
2
3
4
5
0
1000
2000
3000
4000
5000
6000
7000
8000

Figure 7

Distance from fracture center (m)
Fe content (wt%)
δ13C (‰ VPDB)
δ18O (‰ VPDB)
BAB
BAC
BAE
BAG
BAH
Limestone
Bulk dolomite
Fine dolomite
Coarse dolomite
Calcite cement in vugs in dolomite
Weighted (66%) curve fit

Figure 8

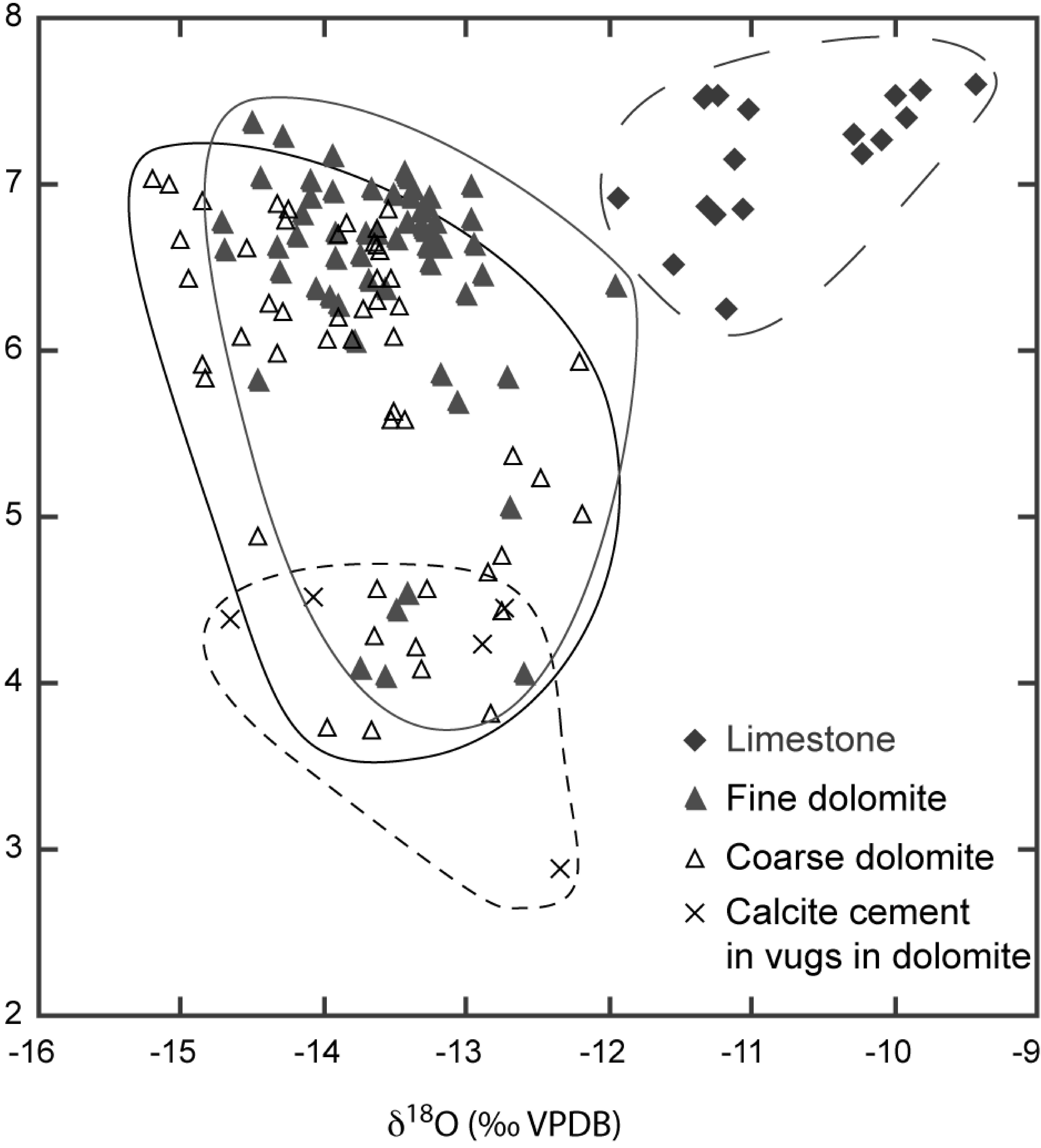

8
7
6
5
4
3
2
-16
-15
-14
-13
-12
-11
-10
-9
$\delta^{13}C$ (‰ VPDB)
$\delta^{18}O$ (‰ VPDB)
Limestone
Fine dolomite
Coarse dolomite
Calcite cement in vugs in dolomite

Figure 9

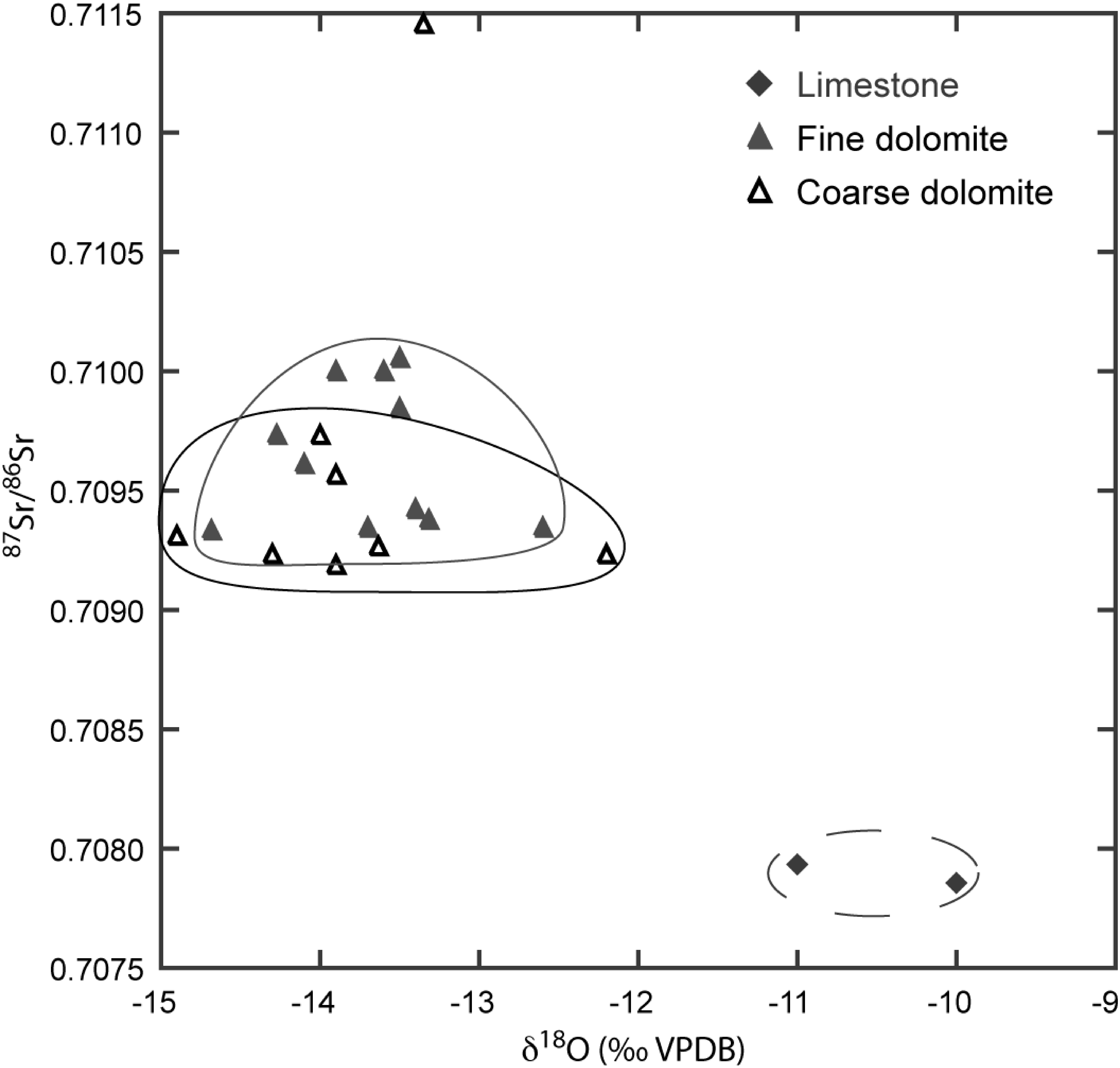

Limestone
Fine dolomite
Coarse dolomite
0.7115
0.7110
0.7105
0.7100
0.7095
0.7090
0.7085
0.7080
0.7075
$^{87}Sr/^{86}Sr$
-15
-14
-13
-12
-11
-10
-9
$\delta^{18}O$ (‰ VPDB)

Figure 10

A
25
20
15
10
5
0
Frequency
Dolomite
Calcite
100
120
140
160
180
200
Homogenization temperature (ºC)
B
35
30
25
20
15
10
5
0
Frequency
Dolomite
Calcite
0
5
10
15
20
25
30
Salinity (wt% NaCl eq)
C
30
25
20
15
10
5
0
Salinity (wt% NaCl eq)
Dol FIA 1
Dol FIA 2
Dol FIA 3
Dol FIA 4
Dol FIA 5
Cc FIA 1
100
120
140
160
180
200
Homogenization temperature (ºC)

Figure 11

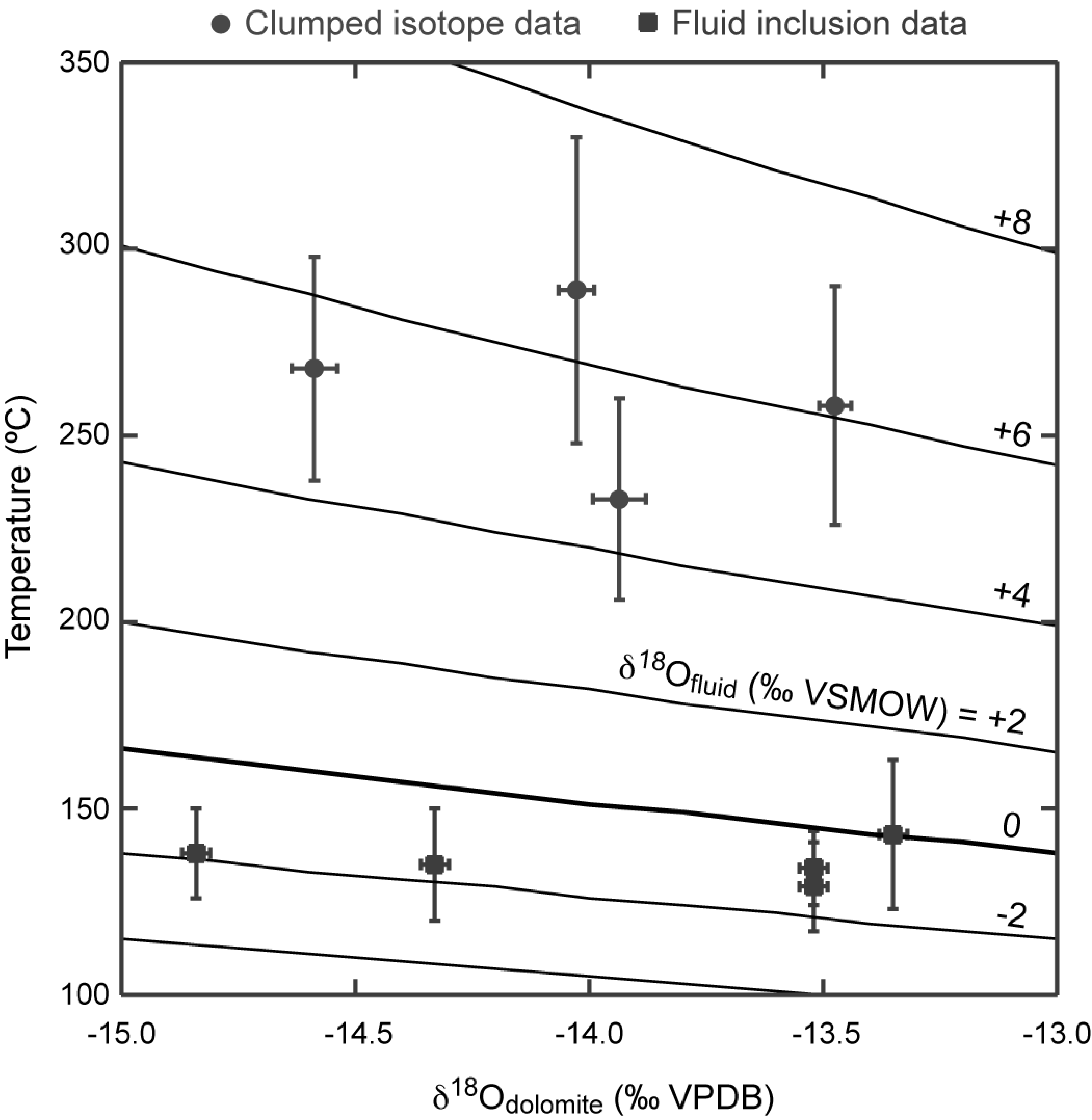

Clumped isotope data
Fluid inclusion data
Temperature (°C)
350
300
250
200
150
100
-15.0
-14.5
-14.0
-13.5
-13.0
$\delta^{18}O_{dolomite}$ (‰ VPDB)
+8
+6
+4
$\delta^{18}O_{fluid}$ (‰ VSMOW) = +2
0
-2

Figure 12


PreC
C
O
S
D
C
P
Tr
J
LK
UK
T
Depth (km)
T (°C)
1
2
3
4
5
6
7
50
80
110
140
170
200
230
Visser (1991)
?
?
Le Nindre et al. (2003)
Saddiqi et al. (2006)
Mount
et al.
(1998)
?
?
600
500
400
300
200
100
0
Time (Ma)

Table 1. Selected examples of dimensions of structurally-controlled dolomite bodies.

Reservoir or outcrop	Location	Host formation	Host age	Dimension	Reference
Stoner Branch locality 11	Central Kentucky	Calloway Creek	Late Ordovician	1200 m away from fault on downthrow side	Black et al. (1981)
Iglesiente-Sulcis mining district	SW Sardinia	Iglesias Group	Early Cambrian	500 km^2 and up to 600 m thick	Boni et al. (2000)
Navain mine	Ireland	Meath	Carboniferous	at least 3 km long, up to hundreds of meters wide and about 150 m thick	Braithwaite and Rizzi (1997)
Clarke Lake	NE British Columbia	Slave Point	Middle Devonian	35 km long and 1-7 km wide	Davies and Smith (2006)
Ladyfern	NE British Columbia	Slave Point	Middle Devonian	15 km long	Davies and Smith (2006)
Albion-Scipio	Michigan	Trenton-Black River	Middle-Late Ordovician	45 km long and up to 1 km wide	Davies and Smith (2006)
Goldsmith-Lakeshore	SW Ontario	Trenton-Black River	Middle-Late Ordovician	15 km long and up to 1.25 km wide	Davies and Smith (2006)
N Gaspé Peninsula	Quebec	West Point	Early Devonian	more than 300 m long	Lavoie et al. (2010)
Asón Valley	N Spain	Ramales platform	Early Cretaceous	km scale long and wide and up to 900 m thick	Lopez-Horgue et al. (2010)
Ranero and El Moro - El Mazo	N Spain	Ranero and El Cuadro	Early Cretaceous	more than 1 km long and up to 30 m wide in El Moro area, but up to 500 m wide in Ranero area	Shah et al. (2012)
Zagros Mountains	Iran	Khami and Bangestan groups	Cretaceous	100 m to several km wide	Sharp et al. (2010)
Wadi Mistal	N Oman	Sahtan Group	Jurassic	about 100 m long, meter-scale wide	Vandeginste et al. (2013)
Deep Panuke	Nova Scotia, Canada	Abenaki platform	Late Jurassic	up to 1 km wide	Wierzbicki et al. (2006)

Taballar River	NE Borneo	Taballar	Oligocene-Miocene	10 km long and 4 to 8 km wide	Wilson et al. (2007)

Sample	Analysis date	Mass spec	Δ48 offset	49 param	$\delta^{18}O$ (‰ VPDB)	$\delta^{13}C$ (‰ VPDB)	Replicate Δ47	Sample Δ47		Temperature (°C)	
BAC4	2-Nov-2013	Pinta	-0.146	-0.115	-14.10	6.39	0.330	0.378	± 0.018	233	± 27
BAC4	22-Nov-2013	Pinta	-1.777	-0.052	-13.90	6.50	0.341				
BAC4	30-Nov-2013	Pinta	-1.346	0.122	-14.02	6.49	0.414				
BAC4	2-Nov-2013	Niña	0.993	0.055	-13.77	6.42	0.420				
BAC4	5-Nov-2013	Niña	0.294	-0.003	-13.89	6.40	0.385				
BAD4	2-Nov-2013	Pinta	-0.311	-0.123	-13.52	6.29	0.313	0.364	± 0.018	258	± 32
BAD4	2-Nov-2013	Niña	1.465	0.032	-13.38	6.36	0.394				
BAD4	5-Nov-2013	Niña	0.460	-0.017	-13.48	6.32	0.360				
BAD4	30-Nov-2013	Niña	1.125	0.199	-13.52	6.26	0.388				
BAH9	2-Nov-2013	Pinta	-0.419	-0.099	-14.03	6.49	0.315	0.349	± 0.020	289	± 41
BAH9	5-Nov-2013	Pinta	-0.273	-0.119	-14.13	6.43	0.315				
BAH9	2-Nov-2013	Niña	1.995	-0.009	-13.94	6.64	0.391				
BAH9	22-Nov-2013	Niña	0.255	-0.003	-14.01	6.55	0.375				
BAJ17	7-Dec-2013	Pinta	-0.672	0.146	-14.62	6.35	0.333	0.359	± 0.016	268	± 30
BAJ17	10-Dec-2013	Pinta	-0.844	0.225	-14.49	6.35	0.358				
BAJ17	11-Dec-2013	Niña	1.143	0.228	-14.65	6.34	0.387				